Materials Science & Engineering A 925 (2025) 147887

Contents lists available at ScienceDirect

Materials Science & Engineering A

journal homepage: www.elsevier.com/locate/msea

Effect of yttrium addition on creep behavior of wrought nickel alloy 718

Rosa Maria Sales da Silveira [a,*], Alessandra Vieira Guimarães [a], Luiz Henrique de Almeida [a], Andersan dos Santos Paula [b], Alexandre Bellegard Farina [c], Loïc Malet [d], Jean Dille [d], Leonardo Sales Araujo [a]

[a] Programa de Engenharia Metalúrgica e de Materiais, Universidade Federal Do Rio de Janeiro, Brazil
[b] Programa de Pós-Graduação Em Ciência e Engenharia de Materiais, Seção de Engenharia de Materiais, Instituto Militar de Engenharia (IME), Brazil
[c] Centro de Pesquisa e Desenvolvimento da Villares Metals S.A., Brazil
[d] 4Mat, Université Libre de Bruxelles (ULB), Belgium

ARTICLE INFO

Keywords:
Yttrium
Rare earth
Alloy 718
Creep rupture

ABSTRACT

The effect of different yttrium addition on the microstructure and creep resistance of alloy 718 was evaluated aiming to obtain superior creep properties. Creep tests were performed and microstructural characterization was carried out on the samples before and after creep, using scanning, transmission and orientation imaging electron microscopy. The results showed that yttrium addition increased the rupture time and decreased the minimum creep rate. It was related to the microstructural changes caused by yttrium, such as the reduction of grain boundary sliding due to the grain growth rate increasing, which generated fewer secondary cracks at the triple points; the decrease in the stacking fault energy of the alloy that difficulted the slip mechanism. Moreover, Y caused the improvement in cohesion and strengthening of grain boundaries, decrease in the initial fraction of δ phase, increase in the fraction of $\Sigma 3^n$ boundaries and the additional contribution to boundary trapping due to precipitation of the Ni_5Y phase.

1. Introduction

718 alloy (UNS N07718) is an austenitic precipitation hardened alloy, widely used as components for high temperature structural components for nuclear, oil & gas and aerospace industries, due to its microstructural stability and excellent creep, tensile and corrosion resistance under high temperature and harsh environments. The high Nb content contributes to the precipitation of Ni_3Nb – γ" phase (tetragonal, DO_{22}), which is the main strengthening phase, together with the $Ni_3(Al, Ti)$ – γ' phase (cubic, $L1_2$). The Ni_3Nb – δ phase (orthorhombic DO_a) may form from γ" phase and/or directly from the matrix, preferentially along the boundaries of the austenitic grains. Additionally, primary (Nb,Ti)(C, N) phases can occur as strings as a result of the thermomechanical processing and the consequent fragmentation of these particles. Its performance is compromised above 650 °C, due to the coarsening followed by dissolution of the γ" phase, favoring the stable δ phase formation, in addition to other phenomena, like oxidation assisted intergranular cracking and dynamic strain aging, that embrittles the alloy [1–4].

In this regard, studies have been dedicated on the application of rare earths in order to improve the mechanical properties and resistance to degrading environments of austenitic alloys [5–8]. Among the rare earths, yttrium (Y) has made an important contribution to improving the strength and oxidation resistance of nickel based superalloys [9]. Most studies are focused on the use of Y on cast or fabricated by additive manufacturing routes [10,11]. However, a precise control of its addition is mandatory, due to its inherent low yield during melting, its tendency to segregate in the interdendritic liquid and to control the formation of phases that can be detrimental to the ductility of the alloy, as the intense precipitation of Ni-Y phases can act as preferential crack nucleation sites [12–14]. Also, Y contributed to increasing the eutectic volume fraction and modifying the carbide morphology. Li et al. [15] identified the $Ni_{17}Y_2$ phase on Ni alloys with 0.05–0.43 wt%Y. The authors observed that the hardness increased up to 0.05 wt%Y, as consequence of the solid solution strengthening by Y, due to its higher atomic radius, in comparison to Ni.

Recent publications investigated the effect of Y on the microstructural evolution and mechanical properties of the alloy 718 produced by additive manufacturing [16–21]. Wang et al. [16] compared the alloy 718 produced by sub-rapid solidification with 0.1 wt%Y against no Y

* Corresponding author.
E-mail address: rosasilveira@metalmat.ufrj.br (R.M.S. da Silveira).

https://doi.org/10.1016/j.msea.2025.147887
Received 27 October 2024; Received in revised form 9 January 2025; Accepted 19 January 2025
Available online 20 January 2025

addition. The authors improved tensile properties of the 0.1 wt%Y alloy and associated it with the refined grain size, due to precipitation of Ni_3Y and $Ni_{17}Y_2$ along the grain boundaries and the higher fraction of δ phase. Palleda et al. [18] investigated the microstructure and high-temperature mechanical properties of alloy 718 over a range of 0–0.58 wt%Y, fabricated by selective laser melting. They observed an increase in the tensile and creep strain for alloys with up to 0.07 wt%Y, due to the Y effect on δ phase morphology and the increase in the grain boundary cohesion. Kakehi et al. [20] also observed the increase of creep rupture life of Y-added alloy 718 produced by selective laser melting, due to the reduced oxygen content by the formation of Y_2O_3 and the suppression of δ phase growth.

However, few studies addressed the Y addition on the wrought alloy 718, for which the behavior at high temperature under creep conditions is not fully understood. Previous work by Guimarães et al. [22] studied the effect of forged and solubilized alloy 718 with 0.05 wt% and 0.6 wt% Y contents on the microstructure and mechanical properties at room temperature. The addition of 0.05 wt%Y contributed to a significant increase in ductility compared to the Y-free alloy, which was associated with the reduction of harmful elements, such as O and S. A higher Y content of 0.6 wt% was harmful for the ductility of alloy 718, due to the intense precipitation of $Ni_{17}Y_2$ particles, which were preferential sites for crack initiation, causing premature brittle fracture. Furthermore, previous work by Silveira et al. [23] evaluated the phase transformation in the forged alloy 718 with the same Y additions and observed that Y alloying was also responsible for a lower δ phase precipitation and decreased the γ" precipitation temperature. It should be emphasized that the resulting wrought microstructure in alloy 718 is remarkably different from the ones obtained by casting and/or additive manufacturing. An impairing factor for the wide use of yttrium as alloying element is its low yield during melting, which can be as low as 15 %. Additionally, Y tends to segregate in the interdendritic liquid and can form phases with relatively low melting points. All these limitations shall be tackled during fabrication of the alloy, such as the Y addition after the deoxidation phases during the melting, as well as the homogenization heat treatment and thermomechanical processing at lower temperatures, in order to avoid the localized melting. However, despite these limitations, the potential for improvement on mechanical properties can significantly outweigh the processing challenges.

To further investigate the Y effect on wrought alloy 718, the present study aims to assess the tensile properties and creep-rupture behavior at 650 °C of a hot rolled alloy 718 modified with two different Y contents, compared to a reference composition, without Y addition. The microstructural evolution before and after creep is discussed. The Y addition increased the creep rupture time, reduced the creep rate and the crack propagation.

2. Experimental procedures

Three ingots were produced by vacuum induction melting (VIM): a reference alloy, with the usual composition (a.k.a. Alloy "A"); and alloys with aimed contents of 0.01 wt%Y (a.k.a. Alloy "B") and 0.07 wt%Y (a.k.a. Alloy "C"), respectively. The melting procedure and the sequence of alloying additions was defined to result in a high Y yield (>60 %) in the melt and low S and O contents of the heats. The ingots were homogenized at 1050 °C and hot rolled at a strain rate of 0.15 s^{-1} (for a true strain of 0.7). The chemical compositions are given in Table 1, where it was evidenced the lower O and S contents for all alloys, even for the no-Y alloy "A", when compared to a previous study of our group [22,23]. The trend of a slight oxygen pick-up and increase in its content for higher Y additions was also evidenced in other works [8,24–26], however, the performance of the alloy is improved, as O and S are effectively and strongly trapped as oxides and oxisulphides. The specimens were encapsulated in quartz under argon atmosphere and annealed at 975 °C for 70 min, water quenched. The two-step aging treatment was performed at 760 °C for 285 min, furnace cooled at 37 °C/h up to 650 °C, held for 65 min and water quenched.

Tensile tests were performed at room temperature at a strain rate of 5 x 10^{-3} s^{-1}. The creep rupture tests were performed at 650 °C and 605 MPa. The tensile specimens presented a gauge length of 26 mm and diameter of 4 mm while the creep specimens had a gauge length of 25 mm and diameter of 6 mm. Two specimens were tensile tested and two creep tested for each alloy.

Microstructural characterization of samples before and after the creep rupture tests were investigated by scanning electron microscopy (SEM), using X-ray energy dispersive spectroscopy (EDS) and electron backscattered diffraction (EBSD) with 20–25 kV on SEM with field emission gun (FEG). Sample preparation for SEM was performed on regions sectioned parallel to the longitudinal axis of the tensile specimen, approximately 1 mm from the fracture, mechanically ground with sandpaper up to 1200 mesh, polished using diamond suspension (6, 3 and 1 μm) and colloidal silica (0.05 μm). Thin foils were prepared by focused ion beam technique and TEM analyses were performed on a Thermo Fisher Talos F200X transmission electron microscope operated at 200 kV.

For the assessment of the grain growth kinetics, samples of the hot-rolled condition were annealed at 1050 °C up to 96 h. This temperature was set to avoid the δ phase precipitation (that would pin the grain boundary migration), therefore, promoting a fast migration rate of the boundaries. After the heat treatment, the samples were ground with sandpaper up to 1200 mesh and polished up to 1 μm and etched with Marble's solution [27]. The grain size measurements were performed on, at least 3 fields for each alloy and based on Heyn linear intercept procedure described in ASTM E112 standard [28]. For comparison, the grains sizes along the time were normalized by the initial grain size for each alloy.

The EBSD scans were post-processed on MTEX toolbox [29]. With a data cleaning procedure to remove noise and misidentifications. The mean grain size was calculated from the EBSD mappings. The grain boundary character distribution was evaluated, with the determination of the low-coincidence site lattice (CSL) boundaries fractions, especially the coherent and incoherent twins ($\sum 3^n$ with n = 1, 2 and 3), were determined according to Brandon criterion [30].

Thermodynamic calculations were made with the Thermo-Calc® software [31] with the thermodynamic database TCNI8 [32], based on the chemical compositions of the alloys. One calculation was made based on the Scheil solidification simulation, assuming complete diffusion in the liquid and restricted diffusion in the solid and microsegregation during solidification. The objective was to assess the Nb and Y segregation in the liquid during solidification and the terminal solidification temperatures for alloys B and C, key to the following processing steps, like the homogenization heat treatment and the thermomechanical processing temperatures (for the complete Scheil diagrams of the Y added alloys, please see the supplementary file). The second calculation was made to consider homogeneous composition and the phases formed along the temperature, more adequate for the post-homogenized

Table 1
– Chemical composition (wt.%) of the produced alloys.

ID Alloy	Ni	Cr	Fe	Ti	Nb	Al	Mn	Si	Mo	C	S	O	Y
A	52.7	17.86	19.61	0.94	5.09	0.55	0.03	0.05	2.99	0.022	0.0017	<0.0010	0.000
B	52.4	17.68	20.68	0.94	5.01	0.40	0.04	0.05	3.01	0.024	0.0020	0.0010	0.011
C	52.7	17.75	19.91	0.93	5.13	0.42	0.03	0.04	3.02	0.025	0.0015	0.0018	0.067

microstructures. The δ phase fraction was calculated from the binarization and thresholding of the backscattered SEM images using shape descriptor maps on BioVoxxel Toolbox from ImageJ.

3. Results and discussion

3.1. Thermodynamic calculations

The thermodynamic calculations were, initially, made to provide the solidus temperatures for the Y-alloyed samples, to properly estimate the homogenization temperature and to assess the formation of the Ni-Y phases and their proportions. The solidus temperature was estimated as ~1150 °C for alloy B and ~1120 °C for alloy C. Furthermore, Fig. 1(a) presents the thermodynamic calculations of the Nb and Y segregation into the liquid during solidification for alloys A, B and C, where a higher segregation potential of Nb and Y is evidenced, especially for alloy C, reaching local concentrations well above the alloying addition. The Nb segregation in the interdendritic liquid may lead to the formation of the Nb rich phases, like primary Nb(C,N), Laves and δ, while the Y segregation is more prominent towards the very end of solidification, resulting the local association with Ni and formation of the Ni-Y phases like Ni_5Y or $Ni_{17}Y_2$ [6,18]. For both Y-added alloys, the calculations based on the Scheil-Gulliver equation, indicated that, during the solidification path, the austenitic matrix (γ), MC carbide ((Nb,Ti)C), Laves (C14), δ (Ni_3Nb) and σ would be formed [33], despite the latter (σ) is rarely evidenced in the as cast structure [34]. For the Y-alloyed samples, in addition to the aforementioned phases, the Ni_5Y was estimated at the end of the solidification. It was observed that the (Nb,Ti)C solidifies before the Y-rich phase, acting as heterogenous nucleation sites, which justify the frequently formation of carbides associated to Ni_5Y. Fig. 1(b) shows the consolidated equilibrium step-cooling diagrams of A, B and C alloys, considering the stable and metastable phases (i.e.: γ′ and γ”). Similar to the Scheil-Gulliver calculations, despite the estimative of the σ phase, it was not considered nor represented in Fig. 1(b), due to the fact that it would occur only under high temperatures and very long timespans than the ones used in this study [35]. No relevant differences between the alloys were observed for the transformation temperatures and mass fraction of phase for the γ-matrix, (Nb,Ti)C, $M_{23}C_6$, δ and γ”. Similar to the Scheil-Gulliver results, the final solidification temperature was lower for the Y-alloyed samples, which is an important information in order to set the appropriate temperature for thermomechanical processing and avoid liquation failure. The γ’ phase showed a slight difference in the precipitation temperature and maximum mass fraction for alloy A due to the higher Al content. For the Y-rich Ni_5Y, the maximum fraction calculated was related to the Y content of the alloy. For alloy B, the maximum fraction was estimated in ~0.10 %, while, for alloy C, the fraction was ~0.28 %.

3.2. Microstructure analysis

Fig. 2 evidences an interdentritic region with Nb and Y segregation and the presence of Nb-rich and Y-rich adjacent particles. The Nb-rich region shows phases as Laves, δ phase and (Nb,Ti)C primary carbides and the Y-rich particle was associated with the Ni_5Y particle, as defined by thermodynamic calculations [18,36].

After the homogenization, thermomechanical processing, solution and aging heat treatments, the primary (Nb,Ti)C particles were evidenced and fragmented as strings, as expected for a hot rolled microstructure and shown in Fig. 3. The refining character of Y for the (Nb,Ti)C particles was revealed, as the mean equivalent diameter of the particles was 5.5 ± 0.5, 4.2 ± 0.4 and 5.1 ± 0.6 μm for alloys A, B and C [22,36]. Also, no Laves particles were revealed, that supports the effectiveness of the homogenization treatments after casting. The δ particles were induced during the sub-solvus solution heat treatment (970 °C), with the precipitation directly from the matrix, mainly along grain boundaries, in order to prevent its growth and, therefore, control final

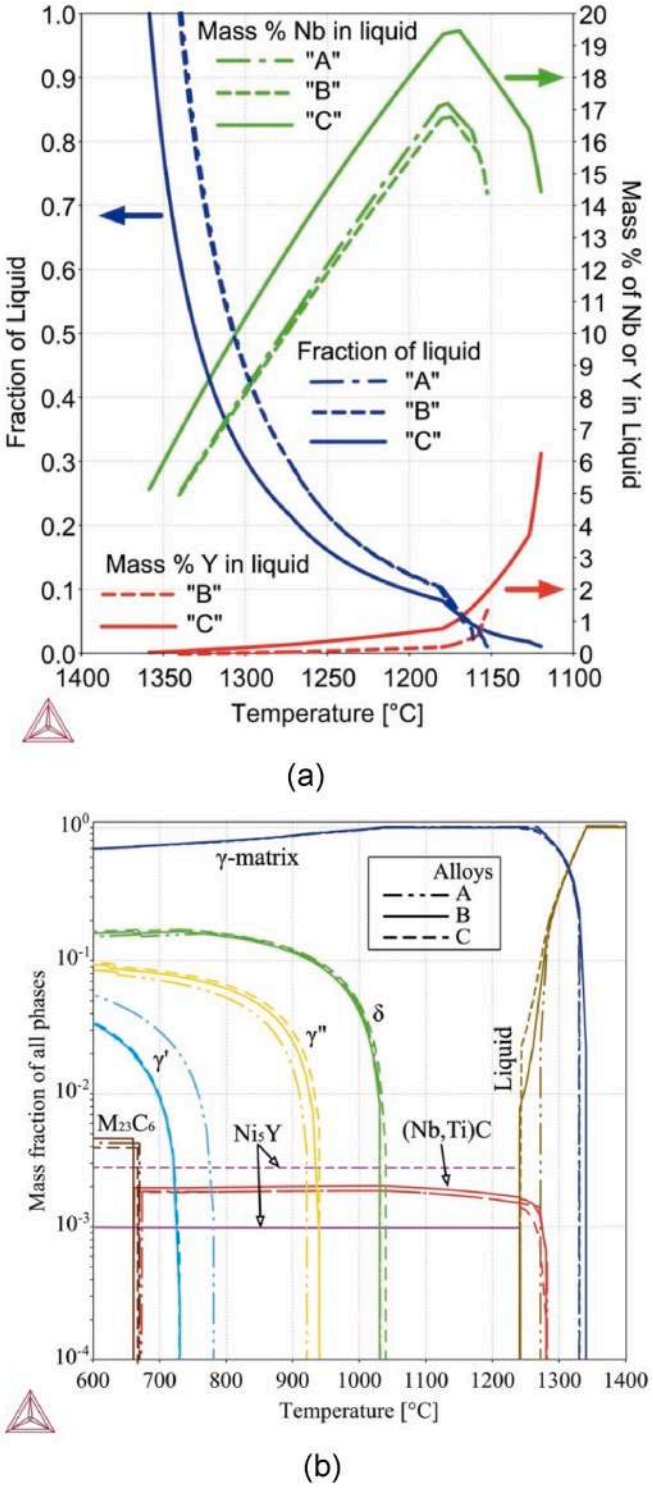

Fig. 1. Thermodynamic calculations for alloys A, B and C: a) Nb and Y segregation through solidification, based on Scheil-Gulliver equation; (b) equilibrium step cooling diagram presenting the mass fraction of the phases formed.

grain size. Yttrium-rich oxides and sulphides were evidenced for samples B and C, corroborating the strong trapping capacity of yttrium. This is an important feature, as it lowers the content of free O and S atoms in the matrix.

Rich Ni-Y particles were identified in both B and C alloys by transmission electron microscopy as Ni_5Y, which has a hexagonal structure with lattice parameters a = 4.883 Å and c = 3.967 Å, as also reported by Palleda et al. [18]. As previously shown, due to the high tendency of

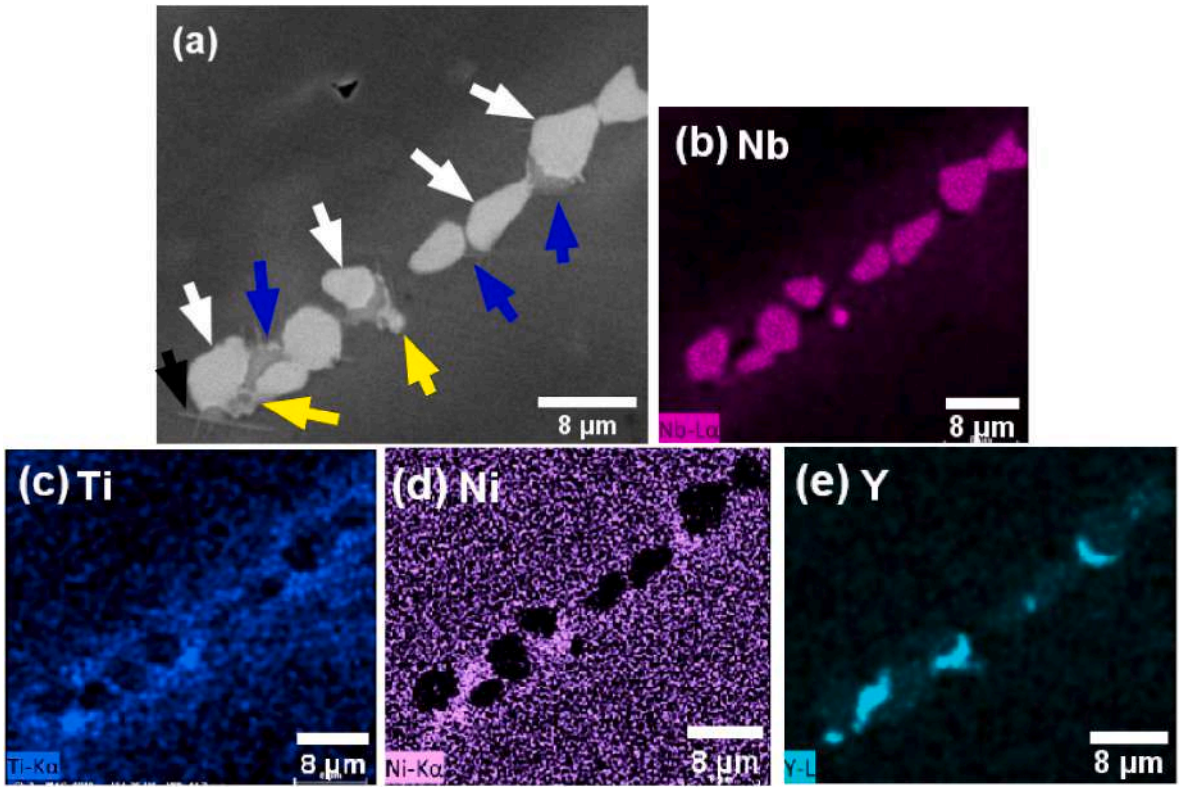

Fig. 2. (a) SEM image of an interdendritic region of the as cast alloy, on backscatter electrons mode, showing (Nb,Ti)C (yellow arrow), thiny δ phase (black arrow), Laves (white arrow) and Ni_5Y phase (blue arrow). The EDS mapping of the as-cast microstructure of sample C is also shown, where (b) Nb, (c) Ti, (d) Ni and (e) Y. (For interpretation of the references to color in this figure legend, the reader is referred to the Web version of this article.)

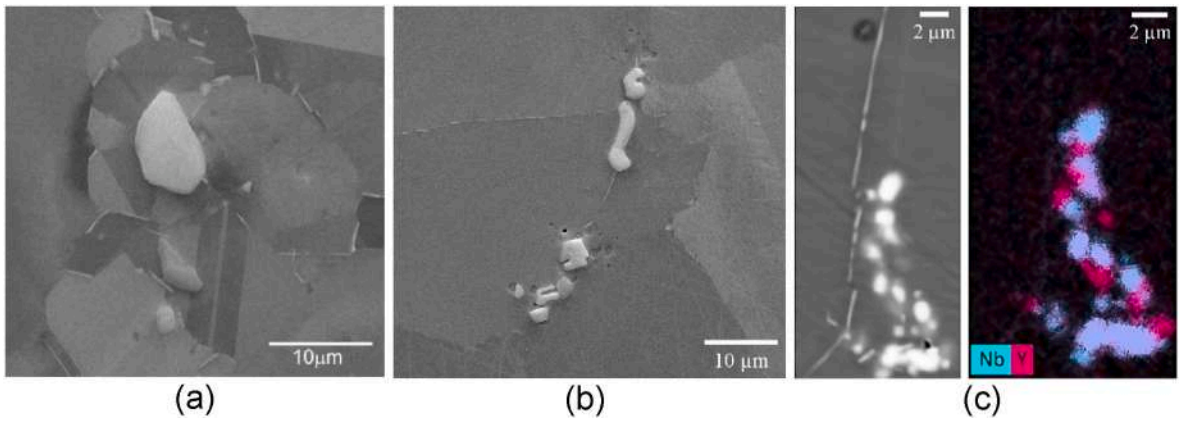

Fig. 3. SEM images of hot rolled samples showing blocky (Nb,Ti)C strings and needle like δ particles of alloys A (a) and C (b) and the presence of Ni_5Y particles on EDS mapping (c) on alloy C.

segregation of yttrium, the Y-rich particles are mainly concentrated within the last solidified regions. Fig. 4 (a) shows the TEM bright-field image of a Ni_5Y particle in alloy B, and Fig. 4 (b) its electron diffraction pattern corresponding to the [2 1 4] zone axis for the Ni_5Y crystal lattice. The size of the main hardening precipitates, γ", was measured from the TEM images along the major axis of the ellipsoidal disks (please, refer to the supplementary file), with average sizes of 28 ± 9, 30 ± 11 and 27 ± 10 nm for alloys A, B and C, respectively. These values were compared to the measurements made by Sundararaman et al. [37]. For the given aging temperature and time, the estimate size of the major axis was of ~30 nm, very close to the present values. The similar sizes of the γ" particles for alloys A, B and C support the close strength values (yield and tensile strength) measured by the tensile tests. Furthermore, Y oxides and sulphides were identified by SEM-EDS, as shown in Fig. 5.

The mean grain size and the area fraction of the δ phase was determined for A, B and C samples after processing and heat treatments. The average grain size was 22 ± 16 µm, 36 ± 26 µm and 34 ± 22 µm, respectively, while the δ phase fraction was 0,46 %, 0.16 % and 0.30 % for alloys A, B and C. It was observed that the grain sizes of the Y-added alloys were larger than the reference alloy A. Fig. 6 presents the grain growth kinetics for the A, B and C alloys, obtained from heat treatments at 1050 °C up to 96 h. As aforementioned, this temperature was defined to avoid the influence of the δ phase on the grain boundary migration. The grain size was normalized from the initial value for each alloy. It can be shown that the Y-alloyed samples showed a higher growth rate than the reference Y-free alloy A.

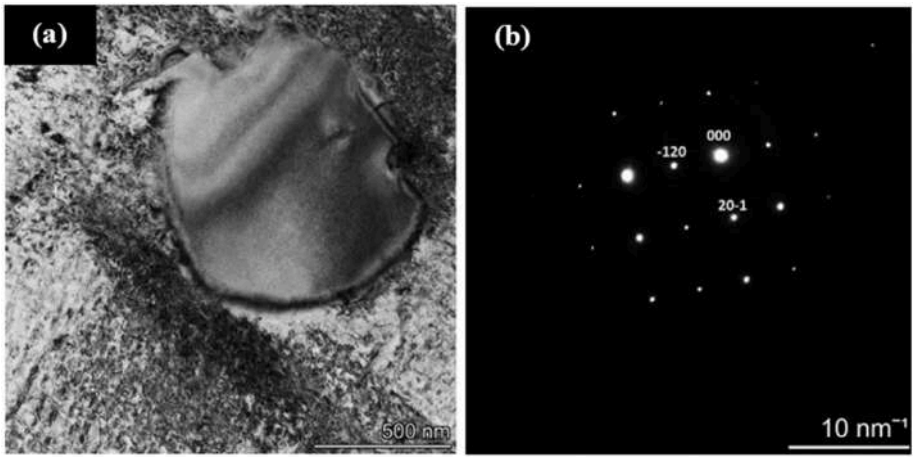

Fig. 4. TEM analysis of a Ni-Y particle in alloy B. (a) TEM bright-field image and (b) electron diffraction pattern corresponding to [214] zone axis for Ni_5Y.

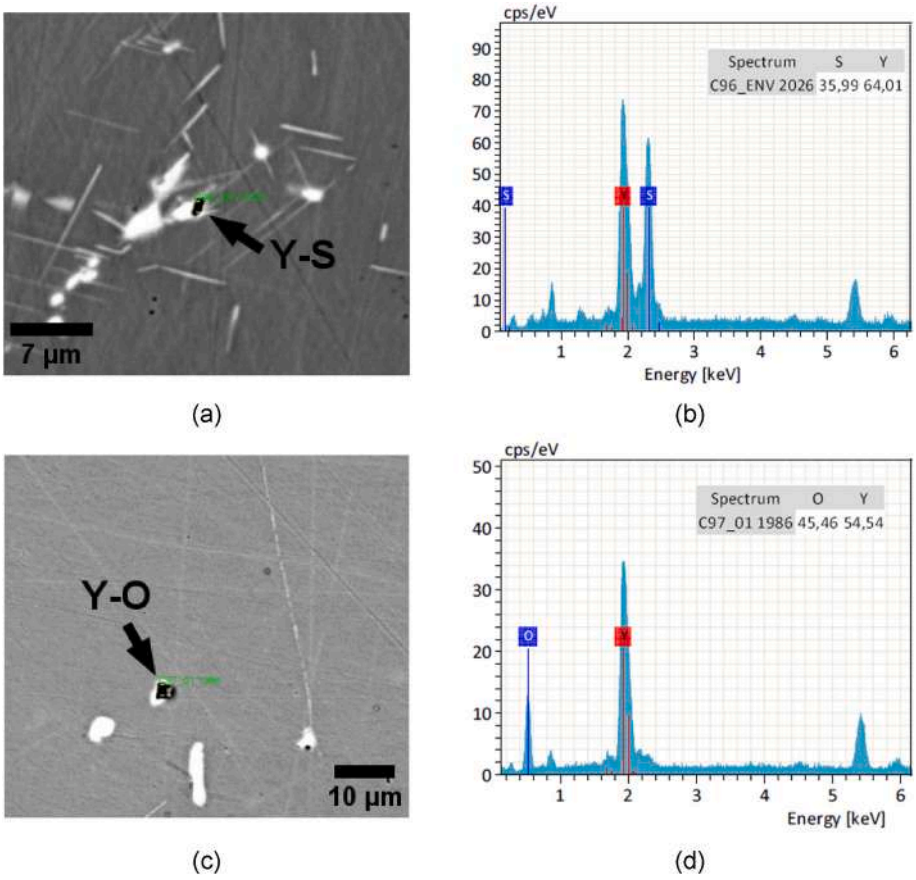

Fig. 5. EDS of Y-rich particles, showing the presence of Y-sulphide and Y-oxide on both alloys B and C.

The grain size during thermomechanical processing can be controlled by the solute drag and/or Zener pinning effects [38]. Impurities as S and O are known to segregate along grain boundaries, which decreases the boundary movement due to solute drag. The Y affinity with these elements will induce the formation of yttrium sulfides and oxides [9], and the concentration of free impurities in the matrix will decrease, despite the overall concentration of S and O did not show an equivalent decrease in the composition measured by spectroscopy. Another point is that Y would interfere in the δ precipitation. The Y atom along grain boundaries would hinder the Nb diffusion, reducing the δ precipitation [8]. This could be corroborated by the lower fraction for the Y-added alloys. The δ phase is important to pin grain boundary movement and, therefore, control the grain size of the matrix. Despite δ precipitation was not the case for tests presented in Fig. 6, as it was conducted above the δ-solvus temperature, its role is relevant for the samples tested for creep and tensile, as the solution temperature was defined as 970 °C, below the δ-solvus, in order to control grain size, a requirement for applications as components for the nuclear power generation. The lower δ fraction for the Y-added alloys was less effective in hindering grain boundary movement during heat treatment. On the other hand, the precipitation of the Ni-Y phase along grain boundary would interfere with the boundary movement, due to the Zener pinning

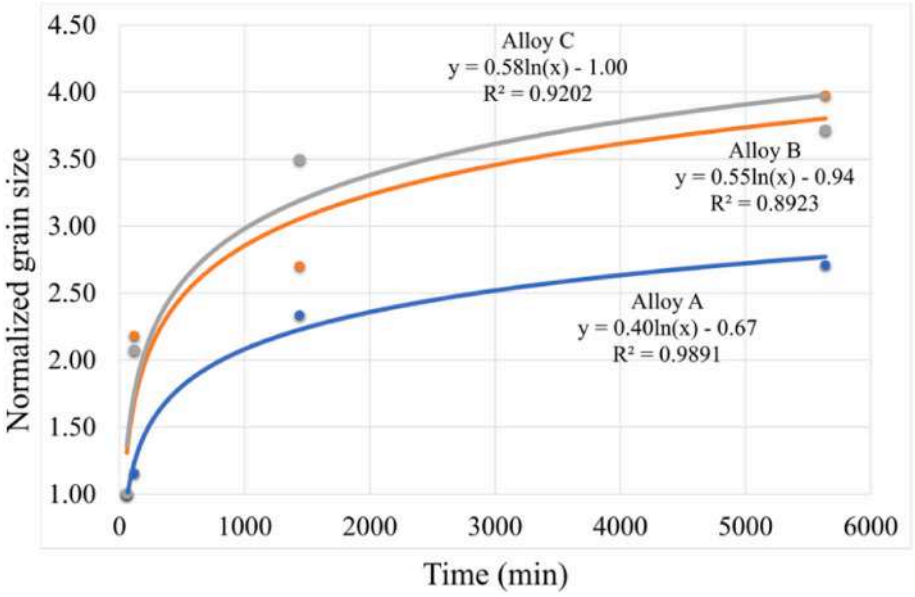

Fig. 6. Grain growth rate at 1050 °C for alloys A, B and C.

effect [39]. Considering the Y-added alloys (B and C), the effect of the former effects was more intense than the limiting effect of the latter, as the growth kinetics were far superior than the reference alloy A (no-Y). Even for alloy C, with the higher Y content, the positive effects on the grain boundary mobility, associated with the Y content, surpassed the Zener pinning effect, as evidenced by the slightly higher mobility, as compared to alloy B.

Fig. 7 shows the IPF maps of the alloys A, B and C, with the colors associated to reference inverse pole figure for face-centered cubic (fcc) structure, and the distribution of $\Sigma3^n$ boundaries ($\Sigma3$, $\Sigma9$ and $\Sigma27$), that are associated with low energy configurations and improved properties [40]. The sum of the length fractions of $\Sigma3^n$ boundaries showed no relevant variations between samples, although a slight decrease with the Y addition was observed, with values of 51.1 %, 46.5 % and 44.2 %, for Alloys A, B and C, respectively. The slightly higher fraction of the no-Y, A sample can be regarded to the thermomechanical processing as, after rolling the, the material was subjected to a heat treatment at 1050 °C for 30 min, in order to complete the recrystallization process, therefore

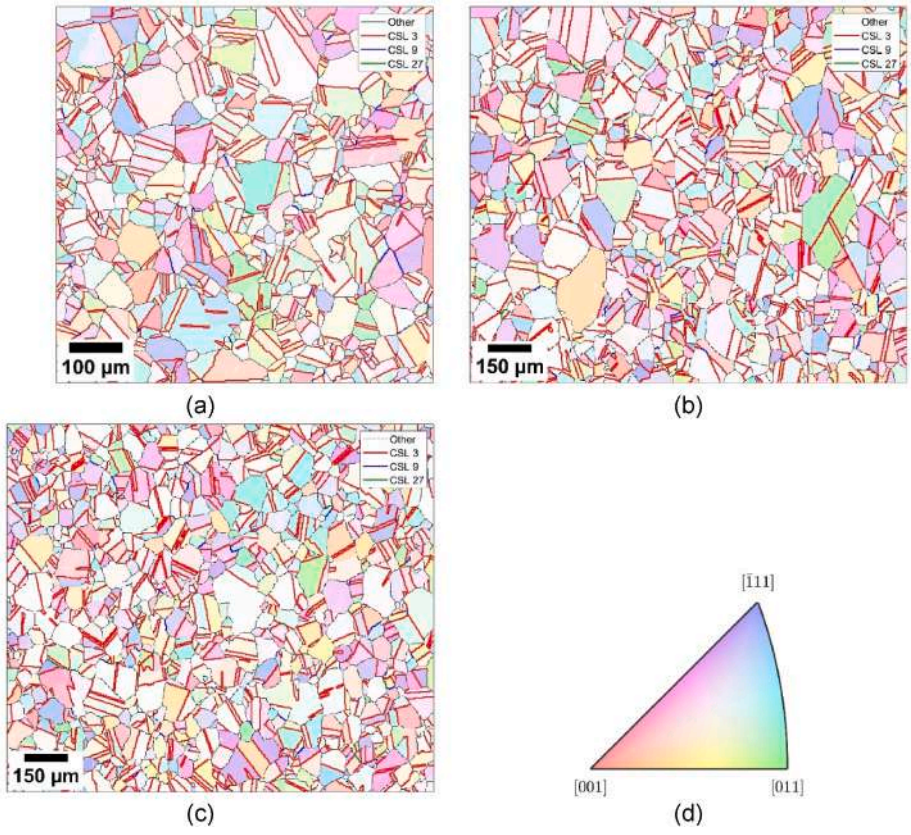

Fig. 7. IPF maps of the alloys A (a), B (b) and C (c), showing the $\Sigma3^n$ boundaries distribution.

permitting more interactions between the $\Sigma 3^n$ boundaries and increasing its fraction [41].

3.3. Mechanical properties

Table 2 describes the mean tensile properties at room temperature, highlighting the ultimate tensile strength (UTS), yield strength (YS) and elongation (el). No relevant variation was observed regarding the strength and ductility between the alloys for the room temperature tensile tests. A positive effect in ductility is associated to the Y alloying, as described in previous works [18,22], as this is linked with the reduction of harmful elements like sulfur and oxygen. For the alloys fabricated for this study, proper attention was given to minimize the content of these harmful elements, as evidenced by the chemical composition presented in Table 1, therefore, no relevant differences were observed for the S and O, as these elements presented very low contents even for the no-Y, reference alloy A. Therefore, no major improvement in room temperature ductility was evidenced due to the Y effect. On the other hand, regarding the creep strength of the alloys, the Y-added alloys (B and C) presented expressive improvements, by increasing the creep rupture time and, consequently, decreasing the average creep rate. For the creep deformation, alloy A showed the highest values, as alloy B presented a considerable decrease in deformation, that were almost fully recovered for alloy C, when compared to the no-Y specimens (A1 and A2 specimens – Fig. 8). Table 3 presents the creep properties of the alloys (time and strain at rupture, and creep rate) and Fig. 8 depicts the creep curves for A, B and C (for each alloy 2 specimens were tested).

The primary stage of creep is relatively short for all three alloys. For the secondary and tertiary creep stages, the longer durations of these stages for B and C alloys becomes evident. Research on additive manufactured samples of Y-alloyed hasteloy X [11] and alloy 718 [36] showed similar improvement on creep properties with Y alloying.

3.4. Analysis of the post-creep specimens

The fractographies of alloys were analyzed by SEM on secondary electron mode and are presented in Fig. 9. It was observed that alloy A (no-Y) showed a typical creep intergranular fracture with some regions containing ductile dimples, as depicted in Fig. 9a to c. The ductile dimples were associated with the decohesion and fragmentation of the precipitates and intragranular δ and (Nb,Ti)C particles. The regions with intergranular fracture facets were decorated with shallow dimples and slip bands, that can be related to the larger creep deformation of alloy A. Fig. 9d to f shows the fracture morphologies of alloy B. Distinct transgranular and intergranular regions were evidenced, but the intergranular facets were dominant, with less prominent indications of slip bands or shallow dimples and the ductile regions presented creep voids along the grain boundaries. Fig. 9g to i depicts the fractography of alloy C, also with a dominant intergranular fracture mode. On the fracture facets, indications of slip and shallow dimples were evident, related to the superior creep deformation when compared to alloy B. In the limited regions with dimple morphologies, creep voids were observed along grain boundaries, like alloy B. It is important to emphasize that the predominance of the intergranular mode increased with the rupture time and yttrium content. The works of Drexler et al. [42] and Asadi et al. [43] presented deformation mechanisms maps for alloy 718. Considering the creep test parameters employed in this study (stress and temperature), the resulting creep rates for alloys A, B and C are close to the threshold value between power law creep and diffusion creep. Therefore, it is indicated that the Y addition gradually changed the main creep mechanism, from controlled by dislocation glide and climb (Alloy A) to controlled by grain boundary migration or stress assisted vacancy migration [43].

Table 2
Mean tensile properties at room temperature.

Alloys	Tensile properties		
	UTS (MPa)	YS (MPa)	el (%)
A	1295 ± 57	1076 ± 78	19 ± 2
B	1296 ± 10	1127 ± 11	16 ± 2
C	1306 ± 11	1097 ± 1	17 ± 1

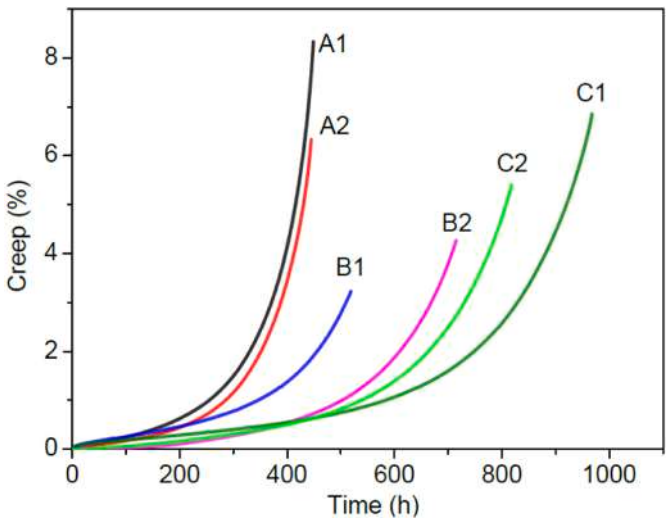

Fig. 8. Creep curves at 650 °C and 605 MPa, for alloys A, B and C. The numbers 1 and 2 indicate the specimens tested.

Table 3
Average creep properties at 650 °C and 605 MPa.

Alloys	t_R (h)	Ɛ (%)	$\dot{\varepsilon}$ (%/h × 10^{-3})
A	398.3 ± 48.8	5.4 ± 2.0	2.3 ± 0.3
B	617.0 ± 98.0	3.8 ± 0.5	1.3 ± 0.6
C	893.0 ± 75.0	6.1 ± 0.7	1.2 ± 0.1

Fig. 10 presents the SEM images of the longitudinal section of the post-creep samples. For all alloys, the cracks emanated from the surface of the specimens. The alloy A (Fig. 10a to c) presented a much higher number of secondary cracks, when compared to the Y-added alloys B and C. These cracks were associated with the linking of the creep voids from the fragmentation and decohesion of the (Nb,Ti)C particles and the δ phase along grain boundaries. Oxidation was evidenced into the cracks, associated with Cr, Al and Fe. As aforementioned, for alloys B and C, although the cracks were associated with similar morphologies as alloy A, its frequency was considerably lower. Along the grain boundaries, the interface of the matrix with the δ particles were more resistant to decohesion and, consequently, increased the resistance to nucleation of voids that could evolve to cracks with time and deformation. For alloy B (9d to 9f), the post-creep samples maintained a morphology of fine δ phase. For alloy C (9g to 9i), its longer time to rupture promoted the transformation of the particles of δ to a needle-like morphology, but this change in morphology did not impact significantly the creep void formation along the interface with the matrix and consequent linking and crack formation and propagation.

The deformation of the post-creep specimens was also investigated by SEM, EBSD and TEM. The deformation was concentrated along the grain boundaries, triple points and the strings of (Nb,Ti)C and, for the Y-added alloys, also around the Ni_5Y particles, leading to stress concentration and void formation due to the fragmentation of the particles and/or decohesion, with consequent evolution to cracks. This was corroborated by the oxide formation on the vicinity of cracks and particles. Fig. 11 shows the voids and the Cr_2O_3 formed on the vicinity of (Nb,Ti)C and δ particles due to the slip bands formed, as well as along grain

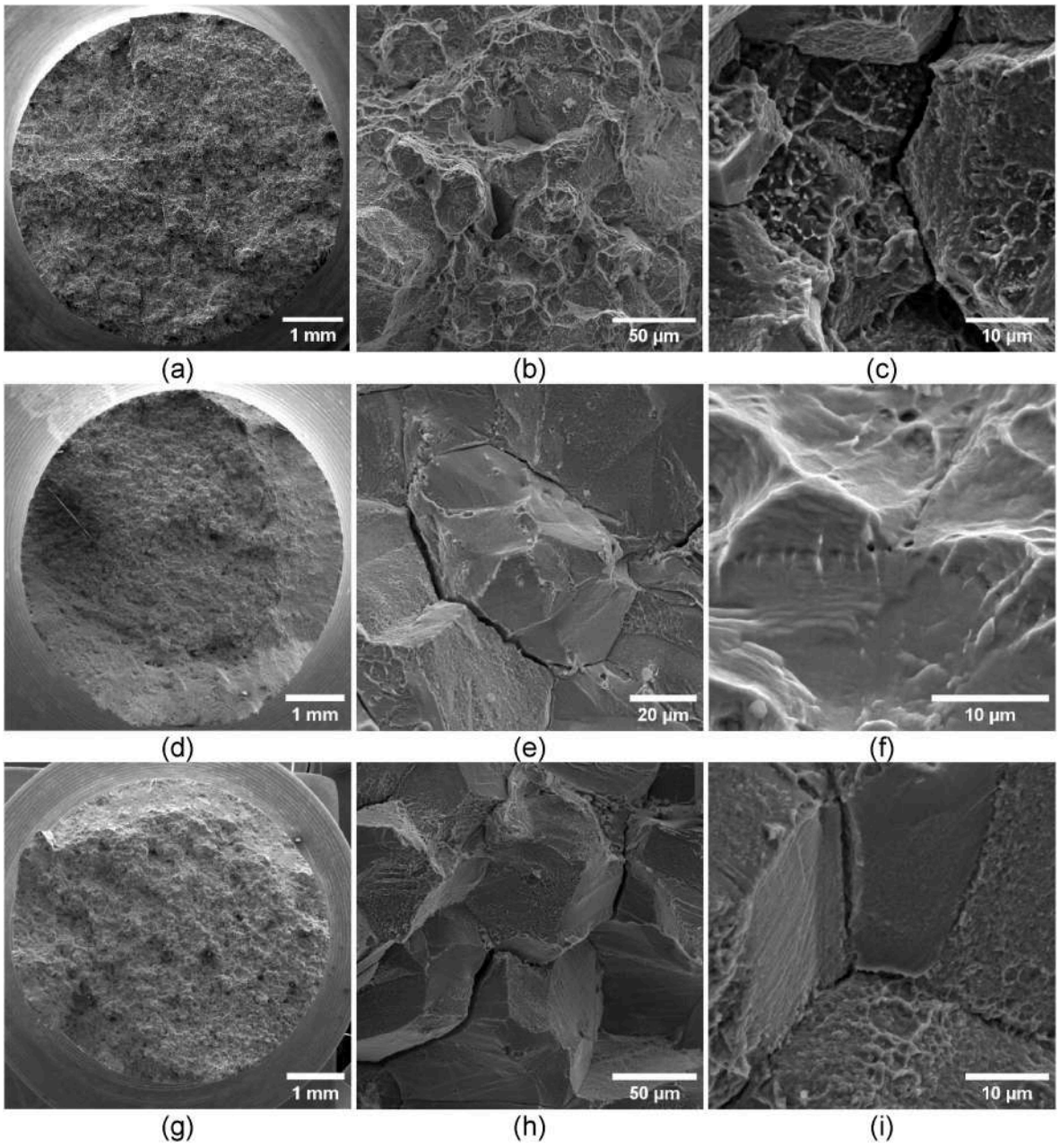

Fig. 9. Fractographs of the creep specimens of alloys A, B and C. Alloy A: (a–c). (a): general view of the fracture; (b): mixed fracture mode (dimples and intergranular); (c): detailed view of the intergranular fracture, with reminiscent ductility on the facets; alloy B (d–f); (d): general view of the fracture; (e): detail of the intergranular fracture with very shallow dimples and secondary cracks; (f): detailed view of the region with dimples, with microvoids formed along grain boundaries; Alloy C (g–i). (g): general view of the fracture; (h): intergranular fracture, with secondary cracks; (i): detail of the intergranular fracture with shallow dimples and slip bands over the facets.

boundaries. The work of Fan et al. [44] showed that the nucleation and growth of Cr_2O_3 is favored in the vicinity of Nb-rich particles. Fig. 12 details the deformation and cracks close to the fracture of the post creep specimen of alloy C. The Image Quality and Kernel Average Misorientation (KAM) maps showed the deformation concentrated along the encounters of the slip bands and grain boundaries, triple points and the strings of second phases like (Nb,Ti)C, δ, and Ni_5Y particles. No secondary cracks were evidenced along the twins and their propagation followed an intergranular path along high angle random boundaries. The deformation inside the grains, due to strain accommodation of regions like triple points and the fragmentation and decohesion of the second phases would contribute to the crack propagation.

Considering the yttrium contents added and the processing of the alloys, it is possible to attest the beneficial effects of the yttrium addition on the creep strength of the alloy 718. Its role on the microstructure can be regarded to various contributions. The initial contribution occurs in the melting process of the alloy. As emphasized in the introduction, yttrium has a strong affinity for oxygen and sulfur, trapping these deleterious elements as oxides (Y_2O_3), sulfides (YS/Y_2S_3) and oxisulfides (Y_2O_2S) [8]. The yttrium addition reduces the content of free O and S atoms in the matrix, which contributes to the cohesion of the matrix-particles interfaces, therefore making the void formation more difficult, which is important to creep stage III, as evidenced especially for alloy C, where the creep deformation was close to alloy A values [45]. Furthermore, the lower content of deleterious elements would favor the cohesion of grain boundaries and their mobility, increasing the

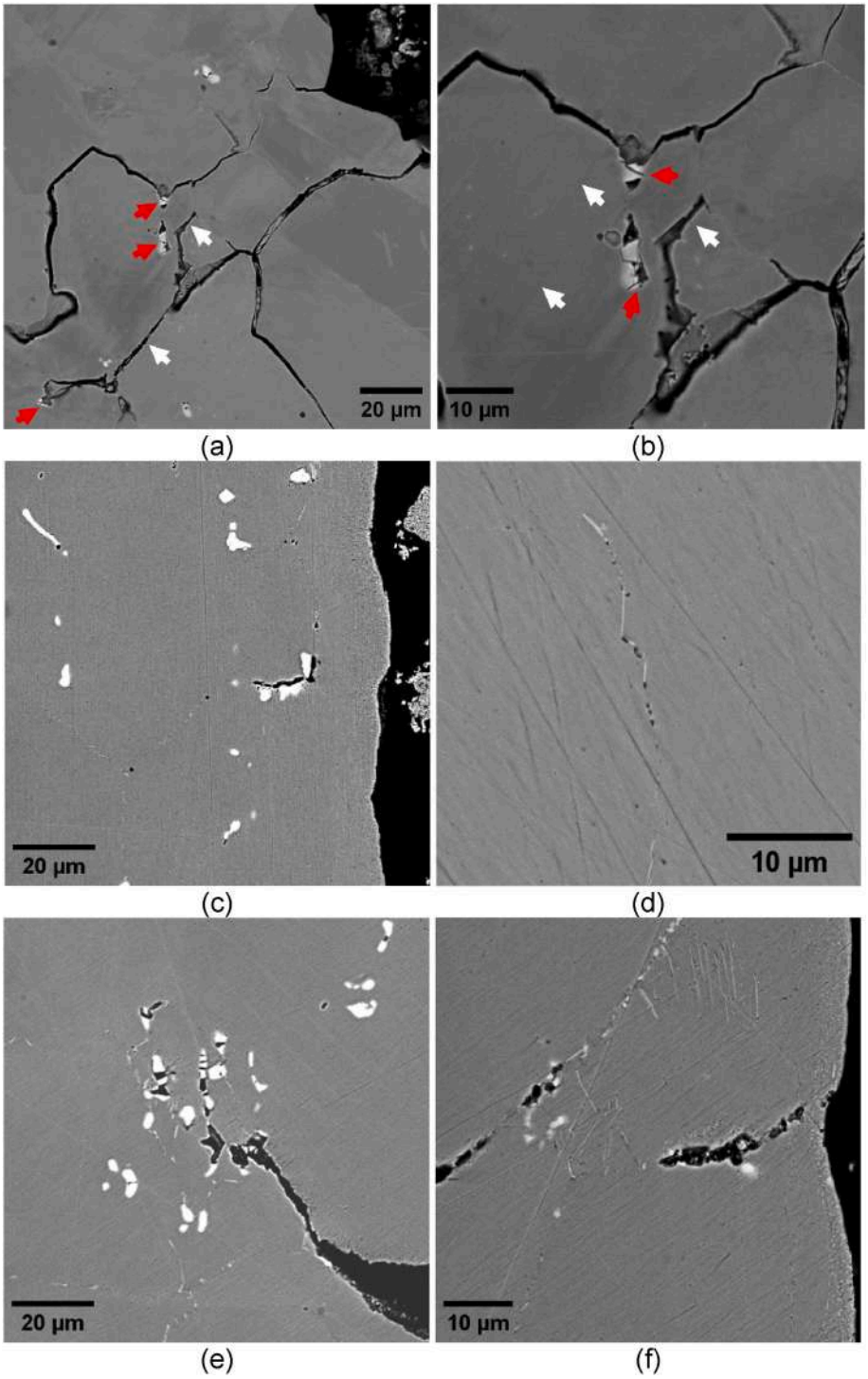

Fig. 10. SEM images of the cracks of the creep specimens of alloys A, B and C. Alloy A: (a–b) showing detail of the cracks, with propagation along grain boundaries. Decohesion of the (Nb,Ti)C particle (red arrow) and slip bands inside the grains (white arrow); Alloy B: (c–d); (c): detail of a secondary crack form from decohesion of the (Nb,Ti)C and voids formed along grain boundaries; (d): micro voids formed along δ phases; Alloy C: (e–f); (e): crack propagation along the grain boundary and decohesion and fracture of a string of (Nb,Ti)C and Ni_5Y particles; (f) The δ particles are evidenced, some with needle like morphology, but with few voids formed along its interfaces. (For interpretation of the references to color in this figure legend, the reader is referred to the Web version of this article.)

resistance to the intergranular cracking [36].

A second important effect of yttrium is on the reduction of the stacking fault energy and, therefore, on the creep properties. Wang et al. [46] showed that Y promoted the reduction of the stacking fault energy (SFE) on the fcc 90Cu10Ni alloy. Tian et al. [47] studied the effect of SFE on creep of Ni-base superalloy with Co addition. They report that the dissociation of a/2 <110> matrix dislocations is predominant over dislocation movement during creep deformation of materials with lower SFE. The dissociation process would be favored by the Suzuki segregation of yttrium in stacking faults promoted by the dissociation, as evidenced in Mg-Zn-Y alloys [48], resulting in the formation of extended stacking faults and microtwins during the secondary and tertiary creep stages. The extended stacking faults and microtwins would difficult cross slip and impose additional barriers to the mobile dislocations,

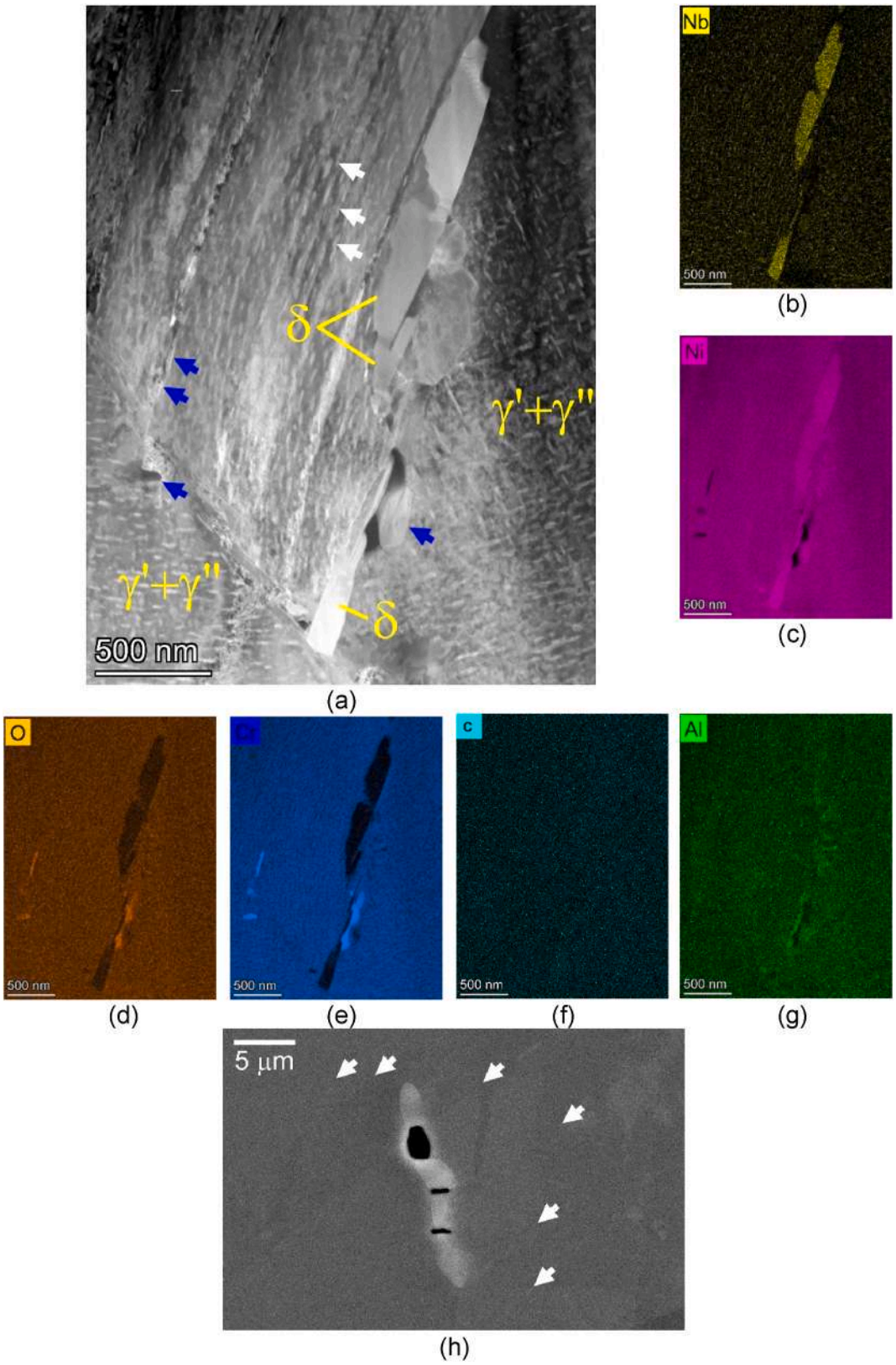

Fig. 11. (a) TEM image on the grain boundary of alloy A with particles of δ and an adjacent chromium oxide particles formed (blue arrows). The white arrows indicate the slip bands; (b–f): EDS mappings: (b) Nb; (c) Ni; (d) O; (e) Cr; (f) C, (g) Al; (h) SEM image of alloy C showing slip bands intersecting a (Nb,Ti)C, with the creep voids formed from fragmentation and decohesion. (For interpretation of the references to color in this figure legend, the reader is referred to the Web version of this article.)

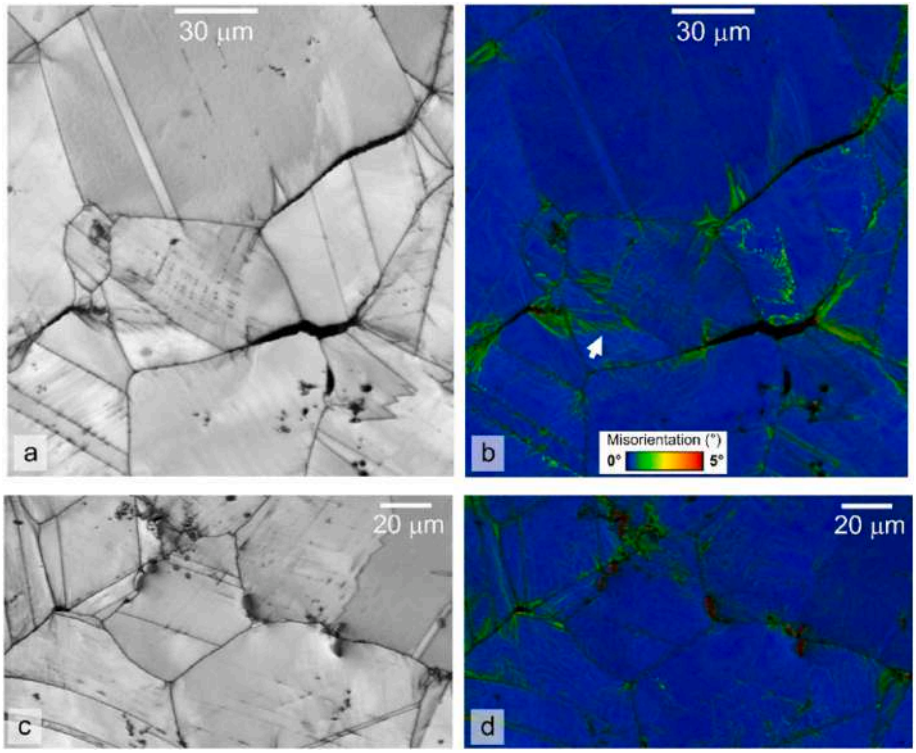

Fig. 12. Image quality (a and c) and Kernel average misorientation maps (b and d) of alloy C, close to the primary fracture. Intense deformation is evidenced at the encounter of slip bands and grain boundaries, around the second phases ((Nb,Ti)C, Ni_5Y and δ) and triple points. The white arrow indicates a region of intergranular deformation, due to accommodation of strain close to a triple point.

therefore increasing the creep strength of the alloy [47].

Another relevant contribution of the yttrium is to change the precipitation of the second phases, like the primary (Nb,Ti)C size and distribution and the fraction of the δ phase, in addition to other phases formed, as Y_2O_3 and Ni_5Y. As already mentioned in this work, the carbide size was refined by the yttrium addition, which was also corroborated by other works [22,36]. These carbides are distributed as intra and intergranular particles and aid the creep resistance of the alloy. Palleda et al. [36] postulated that the (Nb,Ti)C and Y_2O_3 particles interact with moving dislocations, restricting their motion. The authors also evidenced that the carbides promoted serrated grain boundaries, affecting grain boundary sliding. You et al. [49] reported that a high strain is observed around the carbides during creep, which was evidenced in this work (Fig. 12). Fine and distributed particles of the (Nb,Ti)C would reduce local strain concentration and promote a more effective obstacle to dislocations, favoring creep life. The (Nb,Ti)C also presents an important role to difficult grain boundary sliding and hindering dislocation motion, although it may act as a stress concentrator and promote crack formation [20,50]. Despite the lower fraction of δ for the Y-added alloys, its role is still relevant. An appropriate amount of initial δ phase, as obtained in the present work, at the grain boundaries extends rupture time by delaying grain boundary sliding and increasing the extension of stage II [46]. And, due to the longer creep times for alloys B and C, δ is formed from the γ" → δ reaction [36,49,51], with a needle-like morphology, compensating the initial lower fraction.

4. Conclusion

This work studied the effect of adding different amounts of Y to the alloy 718 (0.011 and 0.067 wt%Y) on microstructural evolution and tensile and creep tests, when compared to a reference, no-Y alloy 718. The conclusions are divided into the aspects of Y-effect on the microstructural evolution and the mechanical properties:

Regarding the microstructural evolution:

- The as-cast microstructure showed segregation of Nb and Y into the interdendritic liquid and the formation of adjacent Nb and Ti rich phases as well as Y-rich phases, which can be associated to Ni_5Y. After homogenization and hot rolling, the (Nb,Ti)C and Ni_5Y remained in the microstructure as joint strings. The γ′, γ" and δ were induced through subsequent heat treatment;
- The Y induced the refinement of the (Nb,Ti)C particles and decreased the fraction of the initial δ phase after heat treatment. However, the δ phase was further induced during the creep tests due to the long time and tensile stress;
- The grain growth was faster for the Y-alloyed material, associated with the trapping of S and O, with a reduction of the solute drag effect, increasing the mobility of the grain boundaries. The highest mobility was for alloy with 0.067 wt%Y, indicating that the influence of a higher Y content on the reduction of the solute drag was superior to the potential Zenner pinning from the additional Ni_5Y particles;

With reference to the Y influence on mechanical properties:

- For the room temperature tensile properties, no significant impact was observed for the mechanical properties;
- The creep strength was significantly increased with the Y addition, with the largest increase for the 0.067 wt%Y. The fracture shifted to a predominant intergranular mode, associated with the change of the creep mechanism from power law to diffusion creep. Such improvements were associated with: the decrease in the stacking fault energy of the alloy making slip more difficult; change in (Nb,Ti)C and δ fraction and morphology, as well as precipitation of Ni_5Y and Y sulphides and oxides, providing additional obstacles to dislocation motion and reducing strain localization; increase in the second phases and grain boundaries cohesion.

CRediT authorship contribution statement

Rosa Maria Sales da Silveira: Writing – original draft, Visualization, Validation, Project administration, Methodology, Investigation, Formal analysis, Data curation, Conceptualization. **Alessandra Vieira Guimarães:** Writing – review & editing, Methodology. **Luiz Henrique de Almeida:** Writing – review & editing, Resources, Funding acquisition, Formal analysis, Conceptualization. **Andersan dos Santos Paula:** Writing – review & editing, Methodology. **Alexandre Bellegard Farina:** Writing – review & editing, Resources. **Loïc Malet:** Writing – review & editing, Methodology. **Jean Dille:** Methodology. **Leonardo Sales Araujo:** Writing – review & editing, Supervision, Software, Project administration, Methodology, Investigation, Funding acquisition, Formal analysis.

Declaration of competing interest

The authors declare that they have no known competing financial interests or personal relationships that could have appeared to influence the work reported in this paper.

Acknowledgments

The authors would like to acknowledge the financial support from CAPES, CNPq, FAPERJ and PRH7-ANP. The authors also thanks Villares Metals S.A. for supplying the alloys, IME and 4Mat ULB for EBSD analysis support and CENANO/INT for EBSD and FIB samples preparation.

Appendix A. Supplementary data

Supplementary data to this article can be found online at https://doi.org/10.1016/j.msea.2025.147887.

Data availability

Data will be made available on request.

References

[1] R.C. Reed, The superalloys: fundamentals and applications. https://doi.org/10.1017/CBO9781107415324.004, 2006.
[2] V. Beaubois, J. Huez, S. Coste, O. Brucelle, J. Lacaze, Short term precipitation kinetics of delta phase in strain free Inconel* 718 alloy, Mater. Sci. Technol. 20 (2004) 1019–1026, https://doi.org/10.1179/026708304225019830.
[3] M. Sundararaman, P. Mukhopadhyay, S. Banerjee, Deformation behaviour of γ″ strengthened inconel 718, Acta Metall. 36 (1988) 847–864, https://doi.org/10.1016/0001-6160(88)90139-3.
[4] C. Slama, M. Abdellaoui, Structural characterization of the aged Inconel 718, J. Alloys Compd. 306 (2000) 277–284, https://doi.org/10.1016/S0925-8388(00)00789-1.
[5] D.S. Kang, Y. Koizumi, K. Yamanaka, K. Aoyagi, H. Bian, A. Chiba, Significant impact of yttrium microaddition on high temperature tensile properties of Inconel 713C superalloy, Mater. Lett. 227 (2018) 40–43, https://doi.org/10.1016/j.matlet.2018.03.106.
[6] K. Guan, Z. Huang, R. Cui, J. Qin, Effects of yttrium on microstructure and mechanical properties of a directionally solidified single crystal superalloy, Mater. Sci. Eng. A. 752 (2019) 86–92, https://doi.org/10.1016/j.msea.2019.02.089.
[7] H. Fujikawa, T. Morimoto, Y. Nishiyama, S.B. Newcomb, The effects of small additions of yttrium on the high-temperature oxidation resistance of a Si-containing austenitic stainless steel, Oxid. Metals 59 (2003) 23–40, https://doi.org/10.1023/A:1023061814413.
[8] S. Cao, Y. Yang, B. Chen, K. Liu, Y. Ma, L. Ding, J. Shi, Influence of yttrium on purification and carbide precipitation of superalloy K4169, J. Mater. Sci. Technol. 86 (2021) 260–270, https://doi.org/10.1016/j.jmst.2021.01.049.
[9] K. Di Xu, Z.M. Ren, C.J. Li, Progress in application of rare metals in superalloys, Rare Met. 33 (2014) 111–126, https://doi.org/10.1007/s12598-014-0256-9.
[10] G. Wang, L. Huang, L. Tan, Z. Qin, C. Chen, F. Liu, Y. Zhang, Effect of yttrium addition on microstructural evolution and high temperature mechanical properties of Ni-based superalloy produced by selective laser melting, Mater. Sci. Eng. A. 859 (2022) 144188, https://doi.org/10.1016/j.msea.2022.144188.
[11] S. Banoth, T.N. Palleda, T. Saito, H. Murakami, K. Kakehi, Effects of yttrium and silicon contents in Hastelloy-X built by selective laser melting process, J. Alloys Compd. 896 (2022) 163050, https://doi.org/10.1016/j.jallcom.2021.163050.
[12] P.J. Zhou, J.J. Yu, X.F. Sun, H.R. Guan, Z.Q. Hu, Role of yttrium in the microstructure and mechanical properties of a boron-modified nickel-based superalloy, Scripta Mater. 57 (2007) 643–646, https://doi.org/10.1016/j.scriptamat.2007.06.003.
[13] P.J. Zhou, J.J. Yu, X.F. Sun, H.R. Guan, X.M. He, Z.Q. Hu, Influence of Y on stress rupture property of a Ni-based superalloy, Mater. Sci. Eng. A. 551 (2012) 236–240, https://doi.org/10.1016/j.msea.2012.04.117.
[14] P.J. Zhou, J.J. Yu, X.F. Sun, H.R. Guan, Z.Q. Hu, Roles of Zr and Y in cast microstructure of M951 nickel-based superalloy, Trans. Nonferrous Met. Soc. China (English Ed. 22 (2012) 1594–1598, https://doi.org/10.1016/S1003-6326(11)61361-7.
[15] X.L. Li, S.M. He, X.T. Zhou, Y. Zou, Z.J. Li, A.G. Li, X.H. Yu, Effects of rare earth yttrium on microstructure and properties of Ni-16Mo-7Cr-4Fe nickel-based superalloy, Mater. Char. 95 (2014) 171–179, https://doi.org/10.1016/j.matchar.2014.06.016.
[16] Y. Wang, R. Ran, Y. xiang Zhang, F. Fang, H. song Wang, Y. kun Xia, G. Yuan, G. dong Wang, Effects of yttrium addition on microstructure and mechanical properties of Inconel 718 alloy produced by sub-rapid solidification, Mater. Sci. Eng. A. 823 (2021) 141726, https://doi.org/10.1016/j.msea.2021.141726.
[17] E. Borisov, A. Popovich, V. Sufiiarov, Modification of inconel 718 properties by in situ Y addition in selective laser melting, Materials 15 (2022) 1–9, https://doi.org/10.3390/ma15186219.
[18] S. Palleda, B. Santhosh, M. Tanaka, H. Murakami, K. Kakehi, The Role of Yttrium Micro-alloying on Microstructure Evolution and High-Temperature Mechanical Properties of Additively Manufactured In718, The Authors, 2022, https://doi.org/10.2139/ssrn.4245318.
[19] D.N. Luu, W. Zhou, S.M.L. Nai, Influence of nano-Y2O3 addition on the mechanical properties of selective laser melted Inconel 718, Mater. Sci. Eng. A. 845 (2022) 143233, https://doi.org/10.1016/j.msea.2022.143233.
[20] K. Kakehi, S. Banoth, Y.L. Kuo, S. Hayashi, Effect of yttrium addition on creep properties of a Ni-base superalloy built up by selective laser melting, Scripta Mater. 183 (2020) 71–74, https://doi.org/10.1016/j.scriptamat.2020.03.014.
[21] J.J. Shi, X. Li, Z.X. Zhang, G.H. Cao, A.M. Russell, Z.J. Zhou, C.P. Li, G.F. Chen, Study on the microstructure and creep behavior of Inconel 718 superalloy fabricated by selective laser melting, Mater. Sci. Eng. A. 765 (2019), https://doi.org/10.1016/j.msea.2019.138282.
[22] A.V. Guimarães, R.M.S. Silveira, L.H. de Almeida, L.S. Araujo, A.B. Farina, J.A. F. Dille, Influence of yttrium addition on the microstructural evolution and mechanical properties of superalloy 718, Mater. Sci. Eng. A. 776 (2020) 139023, https://doi.org/10.1016/j.msea.2020.139023.
[23] R.M.S. da Silveira, A. Vieira Guimarães, C.H. de Melo, R.M. Ribeiro, A.B. Farina, L. Malet, L.H. de Almeida, L.S. Araujo, Effect of yttrium addition on phase transformations in alloy 718, J. Mater. Res. Technol. 18 (2022) 3283–3290, https://doi.org/10.1016/j.jmrt.2022.03.137.
[24] W. dong Bian, H. rui Zhang, M. Gao, Q. ling Li, J. peng Li, T. xiang Tao, H. Zhang, Influence of yttrium and vacuum degree on the purification of K417 superalloy, Vacuum 152 (2018) 57–64, https://doi.org/10.1016/j.vacuum.2018.02.031.
[25] W. Bian, H. Zhang, X. Zhang, M. Gao, J. Li, Q. Li, Y. Cui, H. Zhang, Comprehensive influence of Y on K417 superalloy: purification, interactions among the alloy elements and high temperature properties, Mater. Sci. Eng. A. 755 (2019) 190–200, https://doi.org/10.1016/j.msea.2019.04.011.
[26] J.G. Li, N. Wang, J.D. Liu, W. Xu, Influence of rare earth elements (Y, La and Ce) on the mechanical properties and oxidation resistance of nickel-based superalloys: a critical review, J. Mater. Sci. Technol. 195 (2024) 9–21, https://doi.org/10.1016/j.jmst.2023.11.077.
[27] A. International, Astm E-407: standard practice for microetching metals and alloys. https://doi.org/10.1520/E0407-07R15E01.2, 2016.
[28] A. International, ASTM E112-13: Standard Test Methods for Determining Average Grain Size, West Conshohocken, PA, 2013.
[29] F. Bachmann, R. Hielscher, P.E. Jupp, W. Pantleon, H. Schaeben, E. Wegert, Inferential statistics of electron backscatter diffraction data from within individual crystalline grains, J. Appl. Crystallogr. 43 (2010) 1338–1355, https://doi.org/10.1107/S002188981003027X.
[30] D.G. Brandon, The structure of high-angle grain boundaries, Acta Metall. 14 (1966) 1479–1484, https://doi.org/10.1002/pssb.19690310123.
[31] J.-O. Andersson, T. Helander, L. Höglund, P. Shi, B. Sundman, THERMO-CALC & DICTRA, computational tools for materials science, Calphad 26 (2002) 273–312.
[32] TCNI8, Thermo-Calc Software TCNI8, TCS Ni-Based Superalloys Database – Version 8.0, Acessed April, 6, 2019, TCS Ni-Based Superalloys Database, Version 8.0, Acessed March, 5, 2022.
[33] Y. Zhao, K. Li, M. Gargani, W. Xiong, A comparative analysis of Inconel 718 made by additive manufacturing and suction casting : microstructure evolution in homogenization, Addit. Manuf. 36 (2020) 101404, https://doi.org/10.1016/j.addma.2020.101404.
[34] B. Geddes, H. Leon, H. Xiao, Superalloys: Alloying and Performance, ASM International, Ohio, 2010.
[35] S.T. Wlodek, R.D. Field, The effects of long time exposure on alloy 718, in: E. A. Loria, 718 Superalloys (Eds.), 625,706 Var. Deriv., the Minerals, Metals & Materials Society, 1994, pp. 659–670, https://doi.org/10.7449/1994/superalloys_1994_659_670.
[36] T.N. Palleda, H.T. Chowdhury, S. Banoth, H. Murakami, K. Kakehi, Effects of yttrium content on solidification, microstructure, and mechanical properties of laser powder bed fused IN718 superalloy, J. Alloys Compd. 978 (2024) 173404, https://doi.org/10.1016/j.jallcom.2023.173404.

[37] M. Sundararaman, P. Mukhopadhyay, S. Banerjee, Some aspects of the precipitation of metastable intermetallic phases in INCONEL 718, Metall. Trans. A 23 (1992) 2015–2028, https://doi.org/10.1007/BF02647549.
[38] G.W. Hu, L.C. Zeng, H. Du, Q. Wang, Z.T. Fan, X.W. Liu, Combined effects of solute drag and Zener pinning on grain growth of a NiCoCr medium-entropy alloy, Intermetallics 136 (2021), https://doi.org/10.1016/j.intermet.2021.107271.
[39] S. Qiao, S. Liu, N. Li, X. Gao, X. Wen, F. Wang, C. Yuan, Abnormal grain growth in the Ni-based wrought superalloy GH4698 bar during heat treatment, J. Mater. Res. Technol. 30 (2024) 6563–6575, https://doi.org/10.1016/j.jmrt.2024.05.089.
[40] F. Otto, G.B. Viswanathan, E.J. Payton, J. Frenzel, G. Eggeler, On the effect of grain boundary segregation on creep and creep rupture, Acta Mater. 60 (2012) 2982–2998, https://doi.org/10.1016/j.actamat.2012.02.004.
[41] V. Randle, G. Owen, Mechanisms of grain boundary engineering, Acta Mater. 54 (2006) 1777–1783, https://doi.org/10.1016/j.actamat.2005.11.046.
[42] A. Drexler, A. Fischersworring-Bunk, B. Oberwinkler, W. Ecker, H.P. Gänser, A microstructural based creep model applied to alloy 718, Int. J. Plast. 105 (2018) 62–73, https://doi.org/10.1016/j.ijplas.2017.11.003.
[43] M. Asadi, D. Guillot, A. Weck, S.R. Hegde, A.K. Koul, T. Sawatzky, H. Saari, Constructing a validated deformation mechanisms map using low temperature creep strain accommodation processes for nickel-base alloy 718, Am. Soc. Mech. Eng. Press. Vessel. Pip. Div. PVP. 2 (2012) 65–73, https://doi.org/10.1115/PVP2012-78092.
[44] J. kun Fan, H. ci Yang, P. zhe Zhang, J. yu Li, Z. jie Jing, F. long Chen, D. gui Liu, B. Tang, H. chao Kou, J. shan Li, Mechanism of high temperature oxidation of Inconel 625 superalloy with various solution and ageing heat treatment processes, Trans. Nonferrous Metals Soc. China 34 (2024) 3662–3676, https://doi.org/10.1016/S1003-6326(24)66632-X.
[45] R.P. Messmer, C.L. Briant, The role of chemical bonding in grain boundary embrittlement, Acta Metall. 30 (1982) 457–467, https://doi.org/10.1016/0001-6160(82)90226-7.
[46] Z. Wang, C. Song, Y. Zhang, H. Wang, L. Qi, B. Yang, Effects of yttrium addition on grain boundary character distribution and stacking fault probabilities of 90Cu10Ni alloy, Mater. Char. 151 (2019) 112–118, https://doi.org/10.1016/j.matchar.2019.02.040.
[47] C. Tian, G. Han, C. Cui, X. Sun, Effects of stacking fault energy on the creep behaviors of Ni-base superalloy, Mater. Des. 64 (2014) 316–323, https://doi.org/10.1016/j.matdes.2014.08.007.
[48] Z. Yang, M.F. Chisholm, G. Duscher, X. Ma, S.J. Pennycook, Direct observation of dislocation dissociation and Suzuki segregation in a Mg-Zn-Y alloy by aberration-corrected scanning transmission electron microscopy, Acta Mater. 61 (2013) 350–359, https://doi.org/10.1016/j.actamat.2012.09.067.
[49] X. You, G. Dong, Q. Zhang, H. Zhang, T. Cao, H. Zhou, Y. Yiliti, H. Cui, Y. Li, D. Liu, Y. Hu, P. Li, Y. Wang, Investigation of the precipitation behavior and its role on creep deformation and failure mechanisms at high temperatures for a turbine disk alloy, Mater. Char. 210 (2024), https://doi.org/10.1016/j.matchar.2024.113833.
[50] Q. Wang, S. Ge, D. Wu, H. Ma, J. Kang, M. Liu, T. Wang, B. Narayanaswamy, R. Su, Evolution of microstructural characteristics during creep behavior of Inconel 718 alloy, Mater. Sci. Eng. A. 857 (2022), https://doi.org/10.1016/j.msea.2022.143859.
[51] N. Wang, J.D. Liu, W. Xu, J.G. Li, Yttrium induced formation of new pores in an as-cast nickel-based single crystal superalloy, Mater. Char. 215 (2024) 114192, https://doi.org/10.1016/j.matchar.2024.114192.